



3-Aminopropyltriethoxysilane-aided cross-linked chitosan membranes for gas separation: grand canonical Monte Carlo and molecular dynamics simulations

Hossein Riasat Harami¹ · Morteza Asghari^{1,2}

Received: 9 January 2018 / Accepted: 9 January 2019 / Published online: 30 January 2019
© Springer-Verlag GmbH Germany, part of Springer Nature 2019

Abstract

Molecular simulations were performed to consider the structural and transport properties of chitosan/3-aminopropyltriethoxysilane (APTEOS) mixed matrix membranes (MMMs). In order to consider the presence of APTEOS content on the performances of membrane, various amounts of APTEOS were added to the polymeric matrix as a cross-linker. Structural characterizations such as radial distribution function (RDF), fractional free volume (FFV) and X-ray diffraction (XRD) were carried out on the simulated cells. Self-diffusivity and solubility of membranes were calculated using mean square displacement (MSD) and adsorption isotherms, respectively. Additionally, permeability and permselectivity of CO₂ and N₂ gases were calculated by grand canonical Monte Carlo and molecular dynamics methods. The system temperature was set to 298 K using a Nose–Hoover thermostat. According to the results, upon increasing APTEOS loading, CO₂ permeability increases until 10 wt.% loading. Then, by adding 20 wt.% of APTEOS, CO₂ permeability decreases, which could be related to higher crystallinity. XRD graphs indicated that the crystallinity decreased when adding 10 wt.% APTEOS, while higher APTEOS content (up to 20 wt.%) led to higher crystallinity percentage, consistent with permeability results. Compared to literature reports, the present simulation indicated higher accuracy for defining the structural and transport properties of APTEOS cross-linked chitosan MMMs.

Keywords Molecular simulation · APTEOS cross-linked chitosan · Grand canonical Monte Carlo (GCMC) · Molecular dynamics (MD) · Gas separation

Introduction

Membrane gas separation exploiting several types of polymers has recently attracted substantial attention because of low maintenance costs, low energy consumption, high efficiency and also compact procedures [1].

Gas separation using polymeric membrane is a promising industrial process that can be used in a variety of industrial fields such as natural gas sweetening (removal of H₂S and CO₂), separation of hydrogen from ammonia, biogas refinement and separation of oxygen from nitrogen in an airstream.

The crucial factor in increasing the efficiency and applicability of polymeric membranes is a good knowledge of how to enhance the structural and separation properties of polymers. The separation of gas mixtures by polymeric membranes has been scrutinized widely in recent years, with cellulose acetate [2], polysulfone, poly(arylene ether) [3], polyimides [4], being the materials most commonly used.

Knowing the weaknesses and strengths of such processes helps eliminate some of the drawbacks. These membranes suffer from a lack of high separation selectivity and/or permeance and some of them have weak temperature stability. When membrane gas permeance increases, it leads to lower cost of membrane fabrication as it requires less membrane area to separate the same amount of gas, while high selectivity increases the purity of the permeate gas. So, higher gas selectivity and permeability are desirable qualities in the fabrication of polymeric membranes. Polymeric membranes using solution-diffusion mechanisms have indicated a trade-off between permeability and selectivity.

✉ Morteza Asghari
asghari@kashanu.ac.ir

¹ Separation Processes Research Group (SPRG), Department of Engineering, University of Kashan, Kashan, Iran

² Energy Research Institute, University of Kashan, Ghotb-e-Ravandi Ave, Kashan, Iran

In the field of CO₂ separation, apart from poly(vinyl alcohol) blend membrane, researchers have dedicated their full attention to chitosan (CS), another thermally stable biopolymer. A natural semi-crystal polymer, CS is made from chitin. However, CS polymer exhibits low gas permeability due to its unique structure [5]. The molecular weight of CS and degree of deacetylation are 2×10^5 and 90%, respectively [6]. Additionally, it is a biodegradable, flexible, non-toxic and linear amino polysaccharide with a high nitrogen content, which indicates good chemical resistance [7, 8]. CS is a favorable material for improving the mechanical properties of polymers [9]; positive charges exist in the polymeric chain of CS (amino groups), and negative charge comes from other residues in the macromolecule [10]. CS polymer can form intermolecular hydrogen bonds due to its highly reactive groups and rigid D-glucosamine structure [11]. Also, CS demonstrates high hydrophilicity, crystallinity, thin film formation ability and acts as an adhesion material for the isolation of biomolecules.

Xiao et al. [12] studied the permeation of pure CO₂ and N₂ gas through CS membranes cross-linked with trimesoyl chloride, and reported an ideal separation factor of 42. Also, it was pointed out that CO₂ permeability was around 163 Barrer at room temperature. Martínez-Camacho et al. [10] investigated the structural and mechanical properties of CS using sorbitol. They proved that Fourier-transform-infrared (FT-IR) spectra of CS films (see below) show the emergence of a broad peak between 3200 cm⁻¹ and 3570 cm⁻¹, attributed to stretching of OH bonds in the molecule. On the other hand, Despond et al. [13] indicated that humidity affects gas permeation through CS polymer significantly. Moreover, the water permeability coefficient increased greatly with the relative pressure. From another point of view, cellulose, as a competitor of CS, is a mobile low-cost natural polymer. Its facility for structural chemical modification by reaction with available hydroxyl groups make cellulose applicable in a vast range of processes [14]; however, its unique structural and mechanical features allows it to sorb CO₂ gas. When using CS, cross-linking is one of the most important ways of reducing crystallinity and improving ionic transport [15].

The latest novelty in enhancement of membrane morphology to provide sufficient potential for future applications is production of mixed matrix membranes (MMM), which combine the advantages of both organic polymers and inorganic nanoparticles. The two materials chosen for preparation of MMM should be selective, and the inorganic nanoparticle should provide superior selectivity compared with the pristine polymer. Experimental results in the literature confirm that separation characteristics of membranes can be significantly improved by incorporation of only a small percentage of inorganic nanoparticles into the polymeric matrix [16].

One of the most advantageous and useful ways to attain higher permeability and rigidity is the loading of

nanomaterials like metal oxides, metal organic frameworks (MOFs), zeolites, carbon nanotubes and other nanomaterials as filler [17]. In this regard, mesoporous materials, MOFs, polymeric and inorganic membranes, activated carbon, poly(ionic liquids) such as the subclass of polyelectrolytes with ionic repeating unit, silica nanoparticles and covalent organic frameworks (COFs) are some of the typical sorbents used deliberately for CO₂ capture [18–21]. In this wide variety of nanomaterials, zeolite can be considered as one of the most advantageous modifiers, and is utilized extensively in polymeric gas separation. In MMM, a solution-diffusion mechanism controls the permeability (P) as a combined factor stemming from solubility and kinetic diffusivity coefficients. Therefore, gas separation using polymeric membranes is achievable by calculating solubility and diffusivity factors.

The gas selectivity of membranes could be enhanced by using silica nanoparticles, which have a constructive effect on polymeric membranes; silica nanoparticles can effectively increase the selectivity and the solubility of the polar gases through membranes. Furthermore, SiO₂ nanoparticles can diminish the plasticization effect of polymeric membranes by enhancement of polymeric chain interactions and decreasing the thermal motions of chains [22].

Thus 3-aminopropyltriethoxysilane (APTEOS) with 3-aminopropyl and three ethoxysilane groups, or TEOS with four Si-O-C₂H₅ groups, can be applied as a highly efficient additive for cross-linking of CS [23].

Today, thanks to some significant progress in computer hardware and algorithms, molecular simulations can provide accurate understanding of the microscopic mechanisms that affect material performance, and even quantitatively predict desirable properties for complex materials systems of immediate industrial interest.

In recent years, molecular dynamics (MD) simulation has become known as a promising and useful software to estimate the structural characteristics and gas transport properties of systems at a molecular scale [24]. Nowadays, the transport mechanisms of gases within MMMs, and different points of these properties like glass transition temperature (T_g), fractional free volume (FFV), self-diffusivity and solubility coefficients, and X-ray diffraction, have been considered in remarkable detail by means of MD simulation [25]. To the best of our knowledge, MD simulations of CS membranes loaded with APTEOS for gas separation processes have not yet been extensively investigated.

In the current work, CS/APTEOS periodic cells were simulated using Materials Studio 6 software. Structural features, like X-ray diffraction (XRD) and radial distribution function (RDF), and gas separation properties like self-diffusivity (MSD) and solubility (isothermal adsorption), were also investigated. Hence, the consistency of molecular simulation (MS) results and the experimental data of Zargar et al. [26] have been examined and compared.

Computational methods

Theory

In present study, MD simulation was employed to peruse the structural and transport properties of CS/APTEOS membranes. To simulate the constructed membranes, the COMPASS force field, Grand Canonical Monte Carlo (GCMC) and MD methods were used [27]. The main purpose of current investigation was to peruse the gas separation process using MMMs from a microscopic aspect. Specifically, this article pays attention to separation properties such as diffusivity, solubility, permeability and permselectivity, while also considering structural properties like XRD, FFV and RDF of CS/APTEOS membranes loaded with 0, 5, 10 and 20 wt.% of APTEOS. Also, this study explores the influence of APTEOS loading on simulated membrane performance where the system temperature is set to 298 K.

The Monte Carlo (MC) approach is a stochastic way that demonstrative configurations can be built by means of statistical methods. In the MC method, a list of ensembles can be used, such as canonical, isothermal-isobaric, isenthalpic-isobaric, micro-GCMC, which can be placed in order as NVT, NPT, NPH, NVE and μ VT [28]. It is worth noting that, having used realistic and physically unnatural trial moves, the GCMC method was used to attain the results. These trial moves, including rotation, translation, displacement and regrowth, happen according to the system requirements. The GCMC accept or reject the trial moves based on the Metropolis Equation (Eq. 1) as presented below:

$$P_{acc} (o \rightarrow n) = \min \left(1; \exp \left(- \left[U_{(n)} + U_{(o)} / k_B T \right] \right) \right) \quad (1)$$

where U , k_B , $U_{(n)}$ and $U_{(o)}$ are the potential energy, Boltzmann's constant (J/K), the new state potential energy and old state potential energy, respectively.

Permeability of different gases within the dense membranes loaded with various materials can be enlightened by solution-diffusion mechanism. In this mechanism, permeability of component "I" can be estimated as follow (Eq. 2) [50]:

$$P_I = D_I \times S_I \quad (2)$$

In Eq. 2, P_i , D_i and S_i are the permeability coefficient, diffusivity coefficient and the solubility factor of component "i", respectively. Furthermore, the permselectivity of a pair of gases can be computed using Eq. 3:

$$\alpha_{i/\beta} = \left(\frac{D_i}{D_\beta} \right) \times \left(\frac{S_i}{S_\beta} \right) = \alpha_A \times \alpha_B \quad (3)$$

where, $\alpha_{i/\beta}$ hints at the permselectivity of component i over component β by multiplying permdiffusivity (α_A) by permsolubility (α_B) [29, 30].

Materials and periodic cells construction

Periodic cell construction

In the first step, CS polymer chains with 20 repeat units and APTEOS were constructed by Materials Studio 6. Then, using the Forcite module, the energy and geometry of the structures were optimized and relaxed. The raw materials of CS chains and APTEOS are indicated in Fig. 1. Also, CO₂ and N₂ gasses were optimized by geometry optimization to reach their final and clean configurations, as illustrated in Fig. 1.

To build periodic cells loaded with APTEOS, different amount of APTEOS were utilized. The amounts of APTEOS used in each periodic cell are indicated in Table 1. The periodic cells were constructed with ten output frames. Initial cell density and temperature were set at 0.8 g/cm³ and 298 K, respectively. Table 1 indicates the specific names of constructed periodic cells.

The lattice type of all constructed periodic cells was cubic. Subsequently, in order to eliminate local non-equilibrium, all periodic cells were energy minimized by smart task, while the convergence level was set to 0.001 kcal mol⁻¹ Å. Hence, only one configuration of periodic cells was chosen due to the lowest level of energy and the best structure to attain highest performance at the end of simulation. This step accomplished the annealing process. A 200 ps-NVT MD simulation was applied to equilibrate the polymer structures. Then, a 1000 ps-NPT MD simulation at pressure = 1 atm was performed for all of the constructed periodic cells [31, 32]. The average densities resulting from the simulation study are listed in Table 2. The final schematic figures of CS/APTEOS simulated periodic cells are demonstrated in Fig. 1.

Radial distribution function

RDF describes the difference of the particles density as a function of distance. $g(r)$ is formulated in Eq. 4 [33]. RDF or pair correlation function $g(r)$ was applied to peruse alterations in local packing. RDF was also chosen for understanding the distribution of atom in polymers chains built in periodic cells.

$$g(r) = \frac{\rho(r)}{\rho} \quad (4)$$

In this equation, $\rho(r)$ is the local density at distance r . On the other hand, $\langle r \rangle$ in MC simulation can be correlated as Eq. 5:

$$g(r) = \frac{dN(rdr + \delta r)}{\rho 4\pi r^2 dr} \quad (5)$$

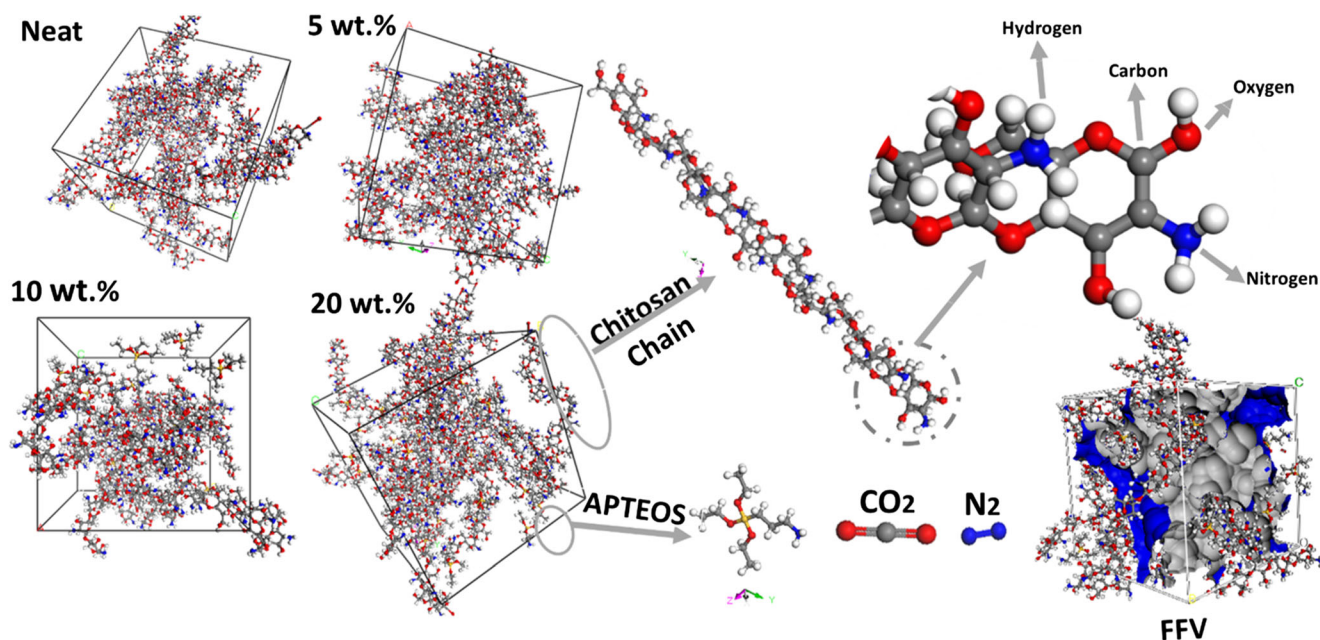


Fig. 1 Molecular dynamics (MD) structure of chitosan (CS) polymer chain, 3-aminopropyltriethoxysilane (APTEOS), gas molecules and constructed amorphous cells and schematic figure of fractional free volume (FFV; blue spaces)

Fractional free volume

Knowledge of free volume helps improve understanding of the mechanism that dominates the penetration of gas molecules within polymer membranes. So, FFVs have been prognosticated from geometrical aspects. A probe was inserted randomly into the periodic cells to measure regions where the probe used has no overlap or contact with any of the fillers or polymer molecules. The FFV is the free volume discerned by a probe with a radius of 0 Å. FFV is essentially a geometric measurement, in that the subtraction of the volume occupied by the polymer chain from the whole cell volume can be expressed as its definition [34, 35]. It is possible to calculate the FFV parameter using Eq. 6:

$$f = \frac{V_1 - 1.3V_w}{V_1} \quad (6)$$

where V_1 is polymer volume and V_w presents the van der Waals volume [36]. The schematic FFV of CS10AP as a sample is depicted in Fig. 1.

Table 1 Specific names of constructed membranes

Sample	Name
Pure chitosan	CS
Chitosan +5 wt.% APTEOS	CS5AP
Chitosan +10 wt.% APTEOS	CS10AP
Chitosan +20 wt.% APTEOS	CS20AP

X-ray diffraction

In MD simulations, XRD allows structural analysis. XRD of constructed cells can be measured based on freely equilibrated structures according to the amount of Cu K(alpha) radiation [37]. In the present article, XRD patterns of CS/APTEOS were obtained from the Reflex Module (Powder Diffraction) in Materials Studio 6.

Diffusion

In MD simulations, particle mobility is evaluated by MSD and can be considered as follow (Eq. 7) [31]:

$$\text{MSD} = \frac{1}{N} \sum_{i=1}^N |\Delta r_i(t)|^2 \quad (7)$$

In Eq. 7, N and $\Delta r_i(t)$ represent particle number. MSD in MD simulation can be calculated from the average of the simulation trajectory. To confirm the MD results, the slope of $\log(\text{MSD})$ graph vs $\log(t)$ has to reach unity [38]. The MSD results calculated for CO_2 at different loading of APTEOS at 298 K are recorded in Table 3. As can be clearly seen, the slopes of the graphs typically approach unity at around 500 ps, proving the reliability of the simulated results.

Sorption (solubility)

To peruse the sorption coefficient of constructed membranes, the GCMC approach was used. The Metropolis algorithm compares the energies of new and existing configurations to

Table 2 Molecular dynamics (MD) details of all simulated periodic cells at 1 atm and 298 K. CS Chitosan, APTEOS 3-aminopropyltriethoxysilane, FFV fractional free volume

Properties	APTEOS wt.% in constructed periodic cells							
	CO ₂				N ₂			
	0	5	10	20	0	5	10	20
Number of CS chains in cells	20	20	20	20	20	20	20	20
Number of APTEOS	0	7	17	37	0	7	17	37
Cell size (Å)	26.74	28.89	32.12	38.19	26.57	28.66	32.09	37.97
Average density (g/cm ³)-298 K	1.243	1.245	1.246	1.249	1.239	1.241	1.245	1.249
FFV	0.2896	0.3021	0.3298	0.3155	0.2889	0.3059	0.3015	0.3019

calculate the equilibrium configuration. A set of ‘moves’ such as creation, deletion and displacement or rotation were attempted in order to choose the best possibility for gas molecules. Totals of 1,000,000 and 100,000 calculation steps were employed as the production and equilibrium steps, respectively. The Metropolis method was employed where the probability of rejecting or accepting a new configuration could be determined from Eq. 8 [39]:

$$probe = \min \left(1; \exp \left(\frac{-\Delta E}{kT} \pm \ln \frac{N_i kT}{f_i V} \right) \right) \quad (8)$$

In this equation, ΔE is the difference of Columbic and van der Waals interactions in two various configurations. Also, k , V , N_i and f_i are Boltzmann’s constant ($J K^{-1}$), the membrane cell volume, number of molecules of component i in the system and the fugacity. A random molecule absorption was applied to deeply consider the rotational displacement in the created membranes. Hence, according to Eq. 9, the sorption coefficient of every single molecule in constructed membrane cells is achievable [40].

$$S = \lim_{p \rightarrow 0} \left(\frac{C}{P} \right) \quad (9)$$

where C and P are the gas concentration and the pressure (fugacity), respectively.

Table 3 Solubility $\{10^{-3} [cm^3 (STP) cm^{-3} (\text{polymer}) cmHg^{-1}]\}$, diffusivity [$10^{-7} (cm^2 s^{-1})$], permeability (barrer) and selectivity of simulated membrane cells at temperature 298 K, 1 atm

APTEOS loading (wt.%)	CO ₂			N ₂			Selectivity P_{CO_2}/P_{N_2}
	Solubility	Diffusivity	Permeability	Solubility	Diffusivity	Permeability	
0	10.12	4.82	48.779	0.89	1.10	0.979	49.825
5	11.32	5.15	58.298	0.95	1.11	1.054	55.311
10	12.93	5.19	67.106	0.83	1.101	0.913	73.500
20	11.69	5.17	60.437	0.88	1.109	0.959	63.020

Results and discussion

Equilibrating periodic cell

In order to validate the thermodynamic equilibrium state, the energy of the constructed cell should be considered. Having applied a 1000 ps NPT run, a promising periodic unit of membrane cells was simulated (Fig. 1) for each sample (CS, CS5AP, CS10AP and CS20AP). The total energy (non-bound energy and potential energy) versus the time step for the CS10AP at temperatures 298 K is illustrated in Fig. 2a. As shown herein, the total potential energy at 298 K starts around 7000 kcal mol⁻¹ then reduces till 5300 kcal mol⁻¹, becoming constant after 200 ps, while the non-bonded energy became fixed at around 6200 kcal mol⁻¹ showing that the system has achieved thermodynamic equilibrium by 1000 ps. Also, the temperature fluctuation was controlled by Nose thermostat to achieve the desired temperature (298 K), as can be seen in Fig. 2b.

Radial distribution function

RDF indicates the relevance of gas concentration as a function of distance (Å) from a specific molecule. Hence, the RDF function was determined in order to peruse the dispersion of APTEOS materials in periodic cells. Additionally, RDF patterns were itemized by membrane types at specific operating

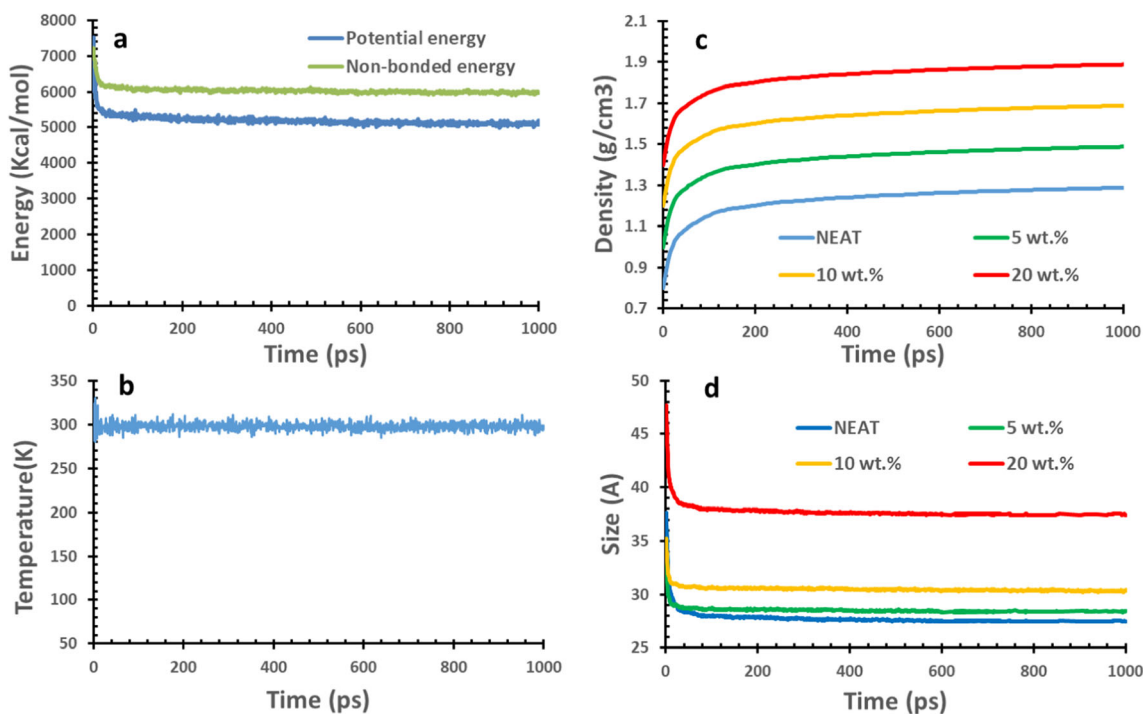


Fig. 2 **a** Non bonded and potential energy fluctuations through MDs versus 1000 ps simulation for CS10AP at 298 K. **b** Temperature fluctuation during 1000 ps, **c** Density diagram of CS/APTEOS for CO₂

(to avoid overlapping, all the graphs were shifted 0, 0.2, 0.4 and 0.6 units higher in the *y*-axis). **d** Cell size diagram (Å) versus duration of NPT run (1000 ps) for CO₂

temperatures. Figure 3a shows the RDF plots of CS membranes. The illustrated patterns for all membranes and (*r*) are nearly the same. At long distances, the pair correlation function differences indicate that there is no long-range order. Hence, all of the simulated configurations can clearly be seen to reach an amorphous state (these results are consistent in approach with the XRD results in Fig. 3b).

Among all RDF patterns, three peaks were manifested. The sharpest and highest peak among the RDF patterns occurs at around $r = 2.38$ Å. This number represents the distance between carbon and the nearest hydrogen atoms. The other obvious peak is around 2.86 Å, which is where the penetrating atoms are most likely to be found. The other peaks revealed at around 4 Å are linked to the carbon atoms' separation from the non-hydrogen atoms, and also the nearest carbon atoms. On the other hand, the CS10AP (10 wt.%) membrane indicated somewhat different behavior compared to other constructed membranes, which could be a key reason behind the difference in gas separation performance. It is worth noting that all the RDF patterns tend to be 1.

XRD graphs

Figure 3b presents XRD graphs of CS membranes at the operating temperatures of 298 K. It is clear that the intensity of the data presented in the current article displays a regularized form as an angle function. As evidenced by the XRD graphs, the degree of crystallinity decreases by adding

10 wt.% APTEOS in the constructed membranes. Also, by increasing the APTEOS content up to 20 wt.%, the degree of crystallinity increases, which is consistent in approach with the gas permeability results. The wavelength was set to 1.54 Å and 2θ was in the range of 0° to 45°. There are two ranges of peaks in 2θ , which are at <5° and ~10°. The XRD pattern can be used to decide between amorphous and crystalline structures. It can be seen that the CS simulated samples consist almost exclusively of amorphous structures. As a consequence, the CS membranes are amorphous, while one sharp peak shows the crystalline part of membranes, which is set around $2\theta < 5^\circ$. Additionally, when the 20 wt.% APTEOS was loaded to membrane, a new peak was created, which proves the higher crystallinity of the CS20AP membrane.

Fractional free volume

The van der Waals distances and cell volumes were calculated for every membrane cell by the means of Connolly surface with a 0 nm-radius probe [41]. Using Eq. 6, FFV was then calculated, as listed in Table 2. The results indicated that an increase in APTEOS content leads to a higher FFV value, which can be related to greater phase separation and membrane cell mobility. Afterwards, by incorporation of 20 wt.% APTEOS material, FFV reduces a bit, as proved by the XRD patterns in Fig. 3b. Therefore, FFV increases with more APTEOS content up to 10 wt.%, at which point gas separation

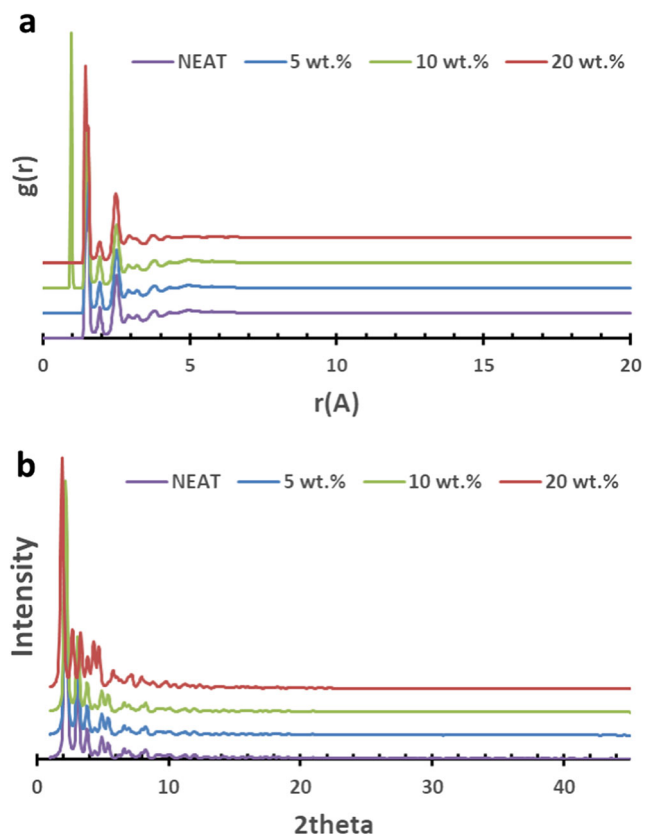


Fig. 3 **a** Total radial distribution function (RDF) for the hard segment of CO₂ at operating temperature of 298 K (in order to eliminate overlapping, CS with 0%, 5%, 10% and 20% of APTEOS profiles were shifted to 0, 0.2, 0.4 and 0.6 units higher). **b** X-ray diffraction (XRD) pattern for CS/APTEOS cells (neat, 5, 10 and 20 wt.%) at operating temperature 298 K and 1 atm

properties improved. Hereafter, loading more APTEOS in polymer matrix up to 20 wt.% caused a reduction in FFV and gas purification performance.

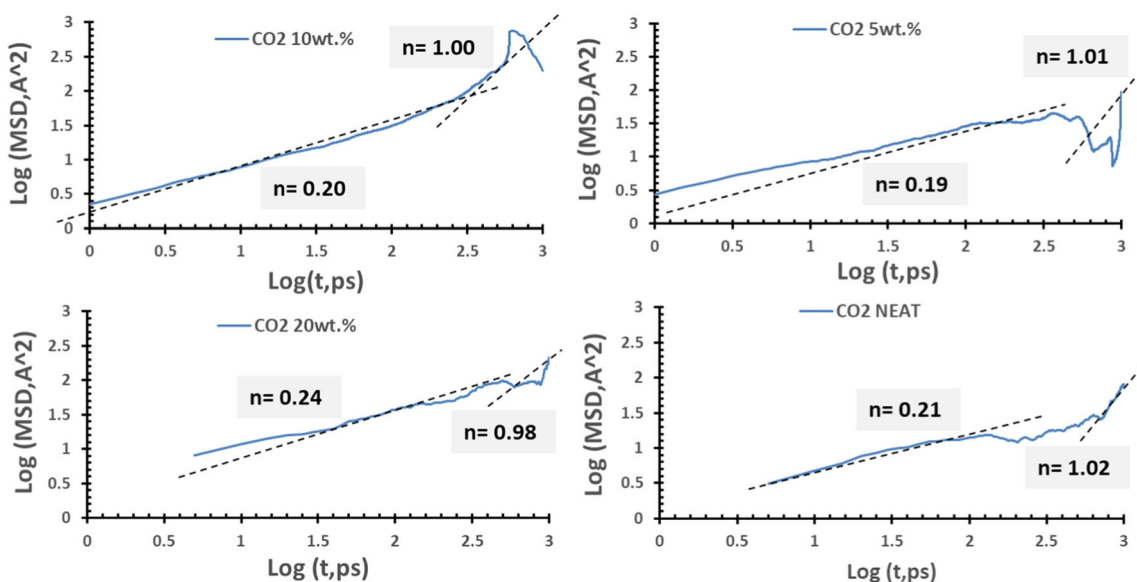


Fig. 4 Log (MSD, Å²) vs. log (time, ps) plot of CO₂ for CS/APTEOS mixed matrix membranes (MMMs) with different content of APTEOS

Density

An example of CS/APTEOS membrane density is shown in Fig. 2c. As shown, the density of membranes alters during NPT MD, but, finally, after applying a 1000 ps-NPT run, all densities become constant. The initial densities of all constructed membranes were set at 0.8 g/cm³. As stated earlier, after 200 ps, the density of membranes turn into constant value for N₂ and CO₂ gases [42]. Besides, having applied an NPT run, the size of the cells created decreases due to the change of density. Hence, the final cell sizes are illustrated in Fig. 2d. As can be seen, the APTEOS augment in constructed membranes causes greater cell size, where CS20AP has the biggest cell. Table 2 lists the average density of the constructed periodic cells containing different amount of APTEOS and CO₂ or N₂ gases. Unfortunately, no experimental data is mentioned in the literature for CS/APTEOS membrane densities to compare with simulation results.

Diffusion, sorption, permeability and permselectivity

Having spread ten molecules of CO₂ and N₂ gases separately in constructed and equilibrated membrane cells, the self-diffusion coefficients (D_i) were calculated using Eq. 7 as mentioned above. These number of gas molecules inserted to the periodic cells was obtained from the literature. By use of the energy minimizer task, the energy of all simulated cells has been minimized. After removing the positions restriction, a 200-ps NVT run was applied with MD methods (Forcite module). The temperature of the system was also controlled by a Nose–Hoover thermostat. Finally, an average value of D_i was calculated from three different and independent states [43]. A 1000-ps NPT MD simulation run was employed over periodic

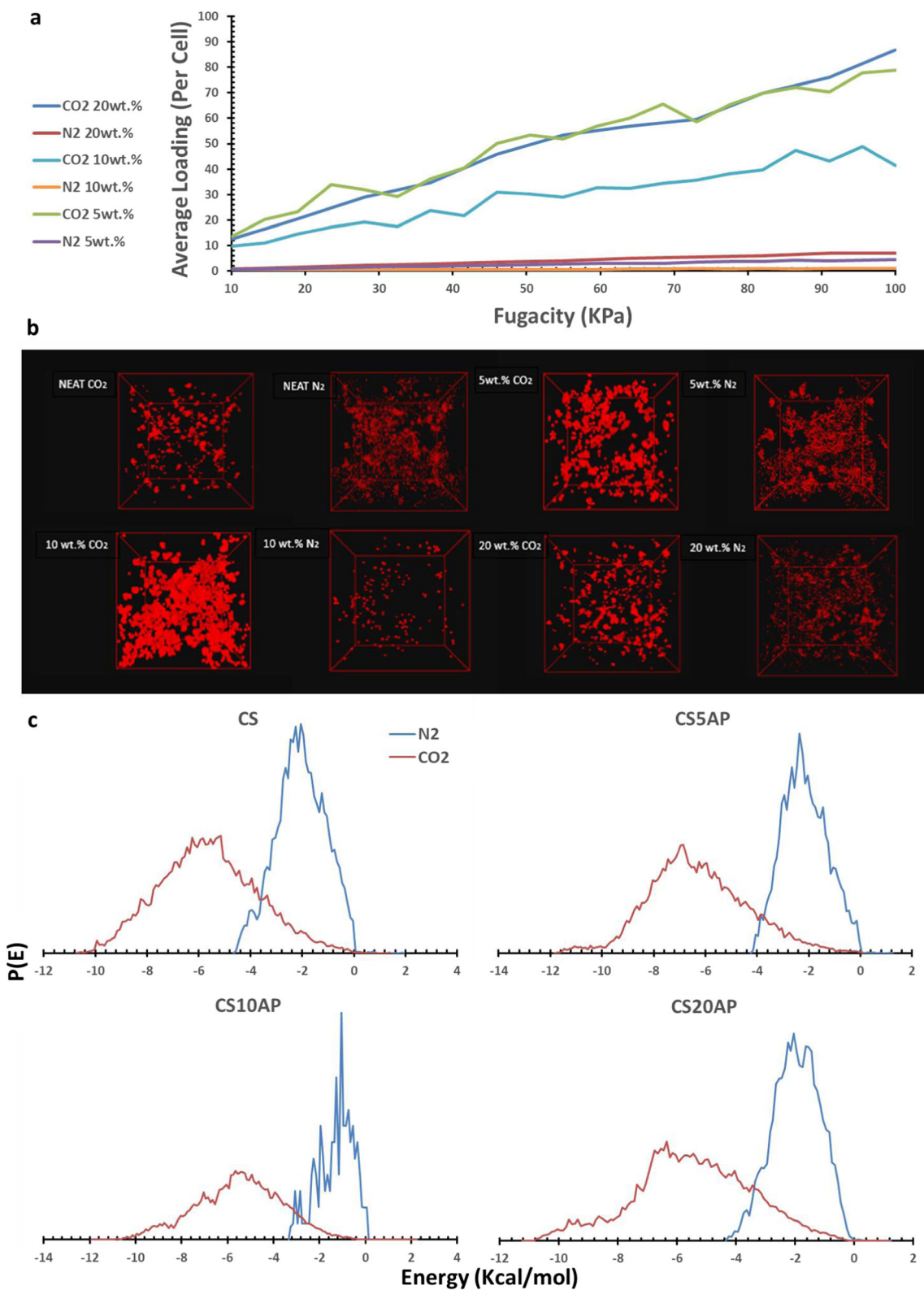


Fig. 5 a Isothermal adsorption task at 298 K and 20 isotherm point of fugacity in the pressures from 0 to 100 KPa for CO₂ and N₂ gases and all simulated membranes. **b** Schematic adsorption of gas molecules within

cells loaded with different APTEOS content to calculate mean square displacement (MSD) of simulated periodic cells. The

the CS/APTEOS MMMs, **c** Adsorption energy distribution of studied gases (CO₂, N₂) in all membranes at 298 K and 1 atm

results obtained are recorded in Table 3. By changing the unit of MSD charts, their slope and afterwards, *D_i* were calculated

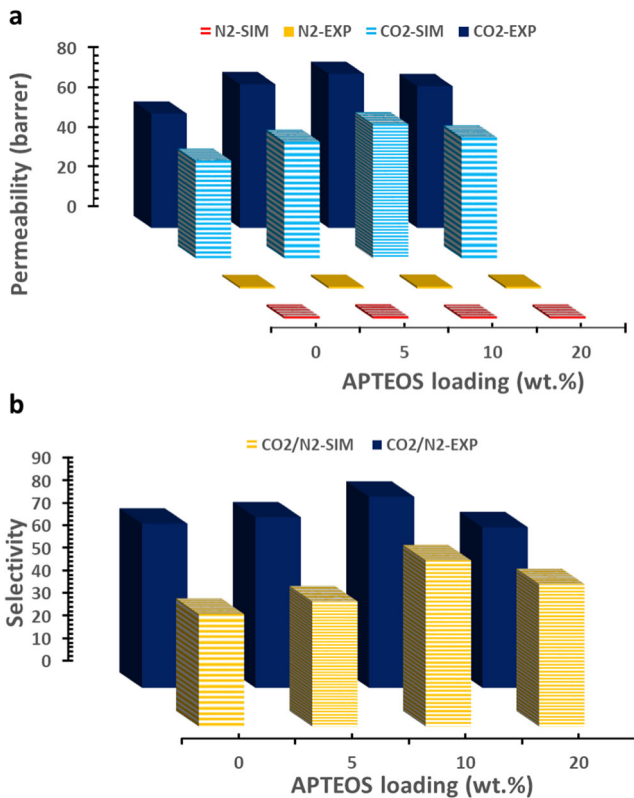
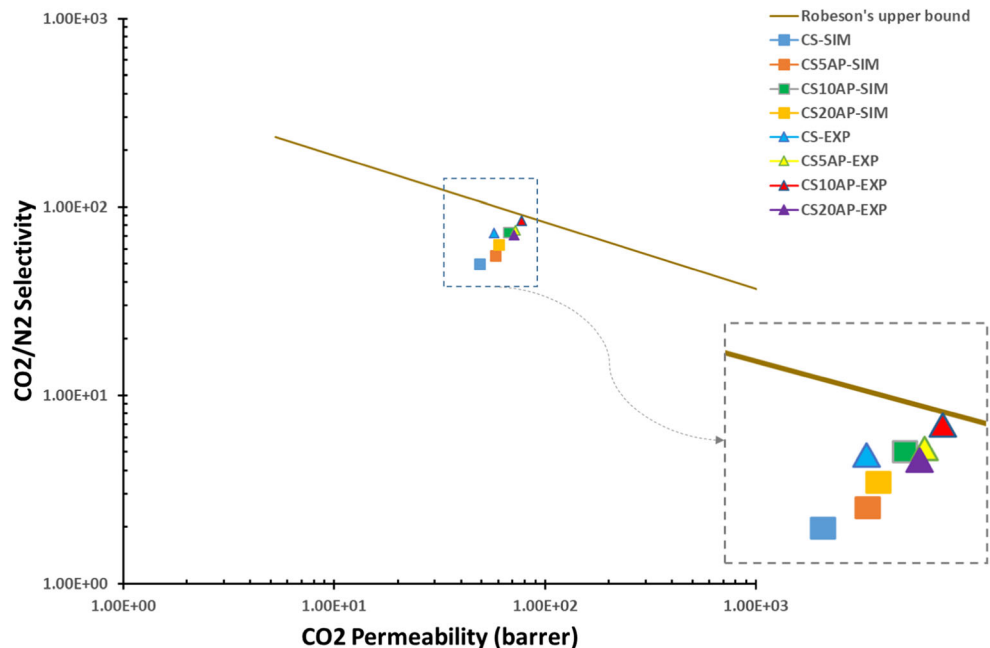


Fig. 6 a Permeability of all simulated membranes for CO₂ and N₂ and its comparison with experimental data. b Selectivity of all simulated membranes and comparison with experimental results [15]

for all configurations containing CO₂ and N₂ gases [44]. To confirm the validity of the results obtained, the standard diffusion coefficient was confirmed, together with the slope of log (MSD) versus log (t) graph, which should achieve unity [31]. These graphs for all MMMs and CO₂ gas are presented

Fig. 7 Robeson's upper bound plot for CO₂/N₂ [46] for all simulated membranes



in Fig. 4. As revealed, the slopes approach unity for all membranes. Thus, the computed self-diffusion coefficients are reliable in this simulation study. As explained before, the transport properties of gas molecules increase by APTEOS loading up to 10 wt.% and reduce with 20 wt.% loading. Obviously, the CO₂ molecule, which is smaller than the N₂ gas molecule diffuses through the CS polymer and APTEOS (which are placed among the polymer chains), while the N₂ gas molecule sticks between the polymer chains due to its bigger molecule.

The other important factor for calculating the permeability of created membranes is solubility, which can be calculated by the Sorption module where the adsorption isotherm task is chosen (GCMC method); 20 altered pressures for 20 isotherm points were fixed. At each fugacity (kPa), 1,000,000 GCMC steps were completed using 100,000 steps-initial equilibration period from 0 to 100 bar for all membranes [45]. Figure 5a shows the graph of isothermal adsorption of N₂ and CO₂ gases from 0 to 100 kPa as fugacity. Solubility coefficients for all periodic cells were calculated and are listed in Table 2. Also, the schematic sites of adsorbed gases within the membranes are depicted in Fig. 5b. As revealed in Fig. 5b, the molecules adsorbed by CS/APTEOS membranes, were placed nearby APTEOS. On the other side, the amount of CO₂ adsorbed within the membranes is more than N₂ gas, which proves that CO₂ solubility is greater than N₂ solubility in value. Concentration and agglomeration of the gas molecules are not very visible, and agglomeration of gas molecules in these sites indicates that the APTEOS existence gives rise higher adsorption. The solubility and diffusivity coefficients of simulation boxes obtained from simulation study are tabulated in Table 3. According to Fig. 5a and b, the solubility of CO₂ molecules increases by APTEOS loading up to 10 wt.% and

then reduces a bit for 20 wt.% loading. It also can be perceived that solubility and diffusivity coefficients for the pair gases are in this order: $\text{CO}_2 > \text{N}_2$. From another aspect, when the CS membrane was loaded with 10 wt.% APTEOS, N_2 permeability decreased compared to other constructed membranes (CS, CS5AP and CS20AP). Additionally, the permeability of CO_2 did not change greatly. But, according to Eq. 3, CS10AP showed a good and reliable permselectivity. Thus, as a result, transport properties and gas separation features of the membranes were improved by increasing the APTEOS content up to 10 wt.%. Also, the equilibration of the system became constant. It is worth stating that, because of a 21-point fugacity diagram, the noise is shown in adsorption isotherm figures. Therefore, the results are obtained from an equilibrated-system, providing accurate and very acceptable adsorption isotherm data.

Also, the actual results of Zargar et al. [26] proved that simulation results are consistent in approach with experiment results. Hence, the gas separation results of CS10AP membrane have good consistency with the results of the current study. Figure 6 demonstrates the permeability and permselectivity of all constructed membranes.

In another aspect, Fig. 5c indicates the adsorption energy distributions containing two sharp and broad peaks at around -6 and -2 kcal mol $^{-1}$ for CO_2 and N_2 gases, respectively. These energy values reveal that the affinity of CO_2 molecules to the CS/APTEOS membranes is higher due to the greater interaction energy of CO_2 with the CS membrane, and, as a result, the CO_2 solubility coefficient is greater.

Robeson's upper bound

Robeson's upper bound represents the performance of the constructed membrane. Regarding membrane permeability and permselectivity, the membranes whose locations are closer to the Robeson's upper bound or may be above the bound indicate higher quality. As demonstrated in Fig. 7, all of the simulated membranes are somehow close to the upper bound, which indicates their high level of quality. For 10 wt.% of APTEOS loading, the CS10AP point became the nearest point to the upper bound graph, which validates this membrane for industry.

Conclusions

In the current study, using Materials Studio 6, molecular simulations to predict the structural and gas separation features of constructed membranes were performed. The COMPASS force field was also employed to explore the diffusivity and solubility coefficients of N_2 and CO_2 gases and also the CO_2/N_2 permselectivity in four different CS/APTEOS membranes loaded with APTEOS contents. Different structural and gas

separation features like RDF, density, FFV and XRD of the constructed membranes have been investigated to characterize the microstructure of the CS/APTEOS membranes.

Gas separation properties of CO_2/N_2 pairs were also investigated in the membrane. X-ray results clearly indicated that membranes with 10 wt.% APTEOS have larger interchain distance than other membranes, and membranes became more amorphous with increasing APTEOS. The membrane with 10 wt.% APTEOS exhibited the best transport properties of all four membrane configurations. This could be related to the fact of phase separation by increasing APTEOS content, where the higher amount of APTEOS causes a wider crystalline region, which reduces gas permeability. So, in CS10AP, more phase separation takes place, which leads to more created pathways for permeation. Furthermore, FFV increases with increasing APTEOS, enhancing membrane transport properties. Moreover, Robeson's upper bound depicts that the simulated membranes have good performance and are qualified for use in industry. This molecular simulation article may provide a new aspect for designing CS/APTEOS membranes to investigate transport and structural properties.

Acknowledgments The authors are grateful to Energy Research Institute at University of Kashan for supporting this work. Also, the authors gratefully acknowledge the computer facilities from High Performance Computing Research Center (HPCRC) in Amirkabir University of Technology (Tehran Polytechnic), Iran, due to the support of this article under the contract number of ISI-DCE-DOD-Cloud-700101-2184.

Publisher's note Springer Nature remains neutral with regard to jurisdictional claims in published maps and institutional affiliations.

References

- Gemeda AE et al (2017) Mixed gas sorption in glassy polymeric membranes. III. CO_2/CH_4 mixtures in a polymer of intrinsic microporosity (PIM-1): effect of temperature. *J Membr Sci* 524:746–757
- Lu HT, Liu L, Kanehashi S, Scholes C, Kentish SE (2017) The impact of ethylene glycol and hydrogen sulfide on the performance of cellulose triacetate membranes in natural gas sweetening. *J Membr Sci* 539:432–440. <https://doi.org/10.1016/j.memsci.2018.03.045>
- Nebipasagil A et al (2017) Polyurethanes containing poly (arylene ether sulfone) and poly (ethylene oxide) segments for gas separation membranes. *Polymer* 118:256–267
- Alaslai N et al (2017) Synthesis and characterization of a novel microporous dihydroxyl-functionalized triptycene-diamine-based polyimide for natural gas membrane separation. *Macromol Rapid Commun* 38(18). <https://doi.org/10.1002/marc.201700303>
- Mi F-L et al (2001) Fabrication and characterization of a sponge-like asymmetric chitosan membrane as a wound dressing. *Biomaterials* 22(2):165–173
- Vijayalekshmi V, Khastgir D (2018) Chitosan/partially sulfonated poly (vinylidene fluoride) blends as polymer electrolyte membranes for direct methanol fuel cell applications. *Cellulose* 25(1):661–681
- Bai R-K, Huang M-Y, Jiang Y-Y (1988) Selective permeabilities of chitosan-acetic acid complex membrane and chitosan-polymer

- complex membranes for oxygen and carbon dioxide. *Polym Bull* 20(1):83–88
8. Ghiggi FF et al (2017) Preparation and characterization of polyethersulfone/N-phthaloyl-chitosan ultrafiltration membrane with antifouling property. *Eur Polym J* 92:61–70
 9. Ghaemi N, Daraei P, Akhlaghi FS (2018) Polyethersulfone nanofiltration membrane embedded by chitosan nanoparticles: fabrication, characterization and performance in nitrate removal from water. *Carbohydr Polym* 191:142–151
 10. Martínez-Camacho A et al (2010) Chitosan composite films: thermal, structural, mechanical and antifungal properties. *Carbohydr Polym* 82(2):305–315
 11. Zubareva A et al (2017) Penetration and toxicity of chitosan and its derivatives. *Eur Polym J* 93:217–223. <https://doi.org/10.1016/j.eurpolymj.2017.04.021>
 12. Xiao S, Feng X, Huang RY (2007) Trimesoyl chloride crosslinked chitosan membranes for CO₂/N₂ separation and pervaporation dehydration of isopropanol. *J Membr Sci* 306(1):36–46
 13. Despond S, Espuche E, Domard A (2001) Water sorption and permeation in chitosan films: relation between gas permeability and relative humidity. *J Polym Sci B Polym Phys* 39(24):3114–3127
 14. Bernard FL et al (2018) Cellulose based poly (ionic liquids): tuning cation-anion interaction to improve carbon dioxide sorption. *Fuel* 211:76–86
 15. Gümüšoğlu T, Arı GA, Deligöz H (2011) Investigation of salt addition and acid treatment effects on the transport properties of ionically cross-linked polyelectrolyte complex membranes based on chitosan and polyacrylic acid. *J Membr Sci* 376(1–2):25–34
 16. Ito A et al (2017) Sulfonated polyimide/ionic liquid composite membranes for carbon dioxide separation. *Polym J* 49(9):671–676
 17. Rezakazemi M et al (2014) State-of-the-art membrane based CO₂ separation using mixed matrix membranes (MMMs): an overview on current status and future directions. *Prog Polym Sci* 39(5):817–861
 18. Bernard FL et al (2017) Hybrid alkoxysilane-functionalized urethane-imide-based poly (ionic liquids) as a new platform for carbon dioxide capture. *Energy Fuel* 31(9):9840–9849
 19. Aquino A et al (2015) Rationalizing the role of the anion in CO₂ capture and conversion using imidazolium-based ionic liquid modified mesoporous silica. *RSC Adv* 5(79):64220–64227
 20. Bernard FL et al (2016) CO₂ capture: tuning cation-anion interaction in urethane based poly (ionic liquids). *Polymer* 102:199–208
 21. Bernard FL et al (2016) New cellulose based ionic compounds as low-cost sorbents for CO₂ capture. *Fuel Process Technol* 149:131–138
 22. Hasebe S et al (2017) CO₂ separation of polymer membranes containing silica nanoparticles with gas permeable nano-space. *J Membr Sci* 536:148–155
 23. Furukawa N, Yamada Y (1997) Preparation and characterization of siloxane-imide block copolymers based on 3, 3', 4, 4'-benzophenonetetracarboxylic dianhydride. *Polym J* 29(11):923
 24. Tocci E et al (2001) A molecular simulation study on gas diffusion in a dense poly (ether-ether-ketone) membrane. *Polymer* 42(2):521–533
 25. Torres J, Nealey P, De Pablo J (2000) Molecular simulation of ultrathin polymeric films near the glass transition. *Phys Rev Lett* 85(15):3221
 26. Zargar V, Asghari M, Afsari M (2017) Gas separation properties of swelled nanocomposite chitosan membranes cross-linked by 3-aminopropyltriethoxysilane. *Int J Environ Sci Technol*:1–10
 27. Sun H, Ren P, Fried J (1998) The COMPASS force field: parameterization and validation for phosphazenes. *Comput Theor Polym Sci* 8(1):229–246
 28. Haario H, Saksman E, Tamminen J (2001) An adaptive Metropolis algorithm. *Bernoulli* 7(2):223–242
 29. Bisoi S et al (2017) Aromatic polyamides containing trityl substituted triphenylamine: gas transport properties and molecular dynamics simulations. *J Membr Sci* 522:77–90
 30. Al-Maythaly BA et al (2017) Tuning the interplay between selectivity and permeability of ZIF-7 mixed matrix membranes. *ACS Appl Mater Interfaces* 9(39):33401–33407
 31. Amani M et al (2014) Study of nanostructure characterizations and gas separation properties of poly (urethane-urea) s membranes by molecular dynamics simulation. *J Membr Sci* 462:28–41
 32. Rahmati M, Modarress H, Gooya R (2012) Molecular simulation study of polyurethane membranes. *Polymer* 53(9):1939–1950
 33. von Lilienfeld OA et al (2015) Fourier series of atomic radial distribution functions: a molecular fingerprint for machine learning models of quantum chemical properties. *Int J Quantum Chem* 115(16):1084–1093
 34. Alentiev AY et al (2014) PIM-1/MIL-101 hybrid composite membrane material: transport properties and free volume. *Pet Chem* 54(7):477–481
 35. Horne WJ, Shannon MS, Bara JE (2014) Correlating fractional free volume to CO₂ selectivity in [Rmim][Tf₂N] ionic liquids. *J Chem Thermodyn* 77:190–196
 36. Golzar K, Modarress H, Amjad-Iranagh S (2017) Separation of gases by using pristine, composite and nanocomposite polymeric membranes: a molecular dynamics simulation study. *J Membr Sci* 539:238–256
 37. Zhang H et al (2010) Response of nanoparticle structure to different types of surface environments: wide-angle x-ray scattering and molecular dynamics simulations. *Phys Rev B* 81(12):125444
 38. Rizzuto C et al (2017) Sorption and diffusion of CO₂/N₂ in gas mixture in thermally-rearranged polymeric membranes: a molecular investigation. *J Membr Sci* 528:135–146
 39. Bakaev V, Steele W (1992) Grand canonical ensemble computer simulation of adsorption of argon on a heterogeneous surface. *Langmuir* 8(1):148–154
 40. Fried J, Goyal D (1998) Molecular simulation of gas transport in poly [1-(trimethylsilyl)-1-propyne]. *J Polym Sci B Polym Phys* 36(3):519–536
 41. Wang Y et al (2017) Structural and water diffusion of poly (acrylamide)/poly (vinyl alcohol) blend films: experiment and molecular dynamics simulations. *J Mol Graph Model* 71:40–49
 42. Ni F, Wang G, Zhao H (2017) Molecular and condition parameters dependent diffusion coefficient of water in poly (vinyl alcohol): a molecular dynamics simulation study. *Colloid Polym Sci* 295(5):859–868
 43. Ambrose RJ et al (2012) Shale gas-in-place calculations part I: new pore-scale considerations. *SPE J* 17(01):219–229
 44. Barrat J-L, Baschnagel J, Lyulin A (2010) Molecular dynamics simulations of glassy polymers. *Soft Matter* 6(15):3430–3446
 45. Luo Y et al (2017) Molecular dynamics simulation insight into two-component solubility parameters of graphene and thermodynamic compatibility of graphene and styrene butadiene rubber. *J Phys Chem C* 121(18):10163–10173
 46. Robeson LM (2008) The upper bound revisited. *J Membr Sci* 320:390–400